






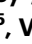



# Million- $Q$ free space meta-optical resonator at near-visible wavelengths

Received: 2 September 2024

Accepted: 21 November 2024

Published online: 28 November 2024

 Check for updates

Jie Fang <sup>1,8</sup> ✉, Rui Chen <sup>1,8</sup>, David Sharp <sup>2,8</sup>, Enrico M. Renzi<sup>3,4</sup>, Arnab Manna<sup>2</sup>, Abhinav Kala<sup>1</sup>, Sander A. Mann <sup>3</sup>, Kan Yao <sup>5</sup>, Christopher Munley<sup>2</sup>, Hannah Rarick<sup>2</sup>, Andrew Tang<sup>1</sup>, Sinabu Pumulo<sup>6</sup>, Yuebing Zheng <sup>5</sup>, Vinod M. Menon <sup>4,7</sup>, Andrea Alù <sup>3,4</sup> & Arka Majumdar <sup>1,2</sup> ✉

High-quality ( $Q$ )-factor optical resonators with extreme temporal coherence are of both technological and fundamental importance in optical metrology, continuous-wave lasing, and semiconductor quantum optics. Despite extensive efforts in designing high- $Q$  resonators across different spectral regimes, the experimental realization of very large  $Q$ -factors at visible wavelengths remains challenging due to the small feature size that is sensitive to fabrication imperfections, and thus is typically implemented in integrated photonics. In the pursuit of free-space optics with the benefits of large space-bandwidth product and massive parallel operations, here we design and fabricate a near-visible-wavelength etch-free metasurface with minimized fabrication defects and experimentally demonstrate a million-scale ultrahigh- $Q$  resonance. A new laser-scanning momentum-space-resolved spectroscopy technique with extremely high spectral and angular resolution is developed to characterize the record-high  $Q$ -factor as well as the dispersion of the million- $Q$  resonance in free space. By integrating monolayer WSe<sub>2</sub> into our ultrahigh- $Q$  meta-resonator, we further demonstrate laser-like highly unidirectional and narrow-linewidth exciton emission, albeit without any operating power density threshold. Under continuous-wave laser pumping, we observe pump-power-dependent linewidth narrowing at room temperature, indicating the potential of our meta-optics platform in controlling coherent quantum light-sources. Our result also holds great promise for applications like optical sensing, spectral filtering, and few-photon nonlinear optics.

High-quality ( $Q$ )-factor optical resonators with ultranarrow spectral linewidth ( $\Gamma_\omega = \omega_0/Q$ , where  $\omega_0$  is the resonance frequency) play a crucial role in modern photonics and quantum optics<sup>1,2</sup>, facilitating extreme temporal coherence<sup>3</sup>, with lifetime on the time scale of  $-Q/\omega_0$ . Numerous essential applications, including optical frequency combs<sup>4,5</sup>, monochromatic lasers<sup>6,7</sup>, low-photon-number nonlinear optics<sup>8</sup>, unidirectional nano-emitters<sup>9</sup>, and cavity quantum electrodynamics studies<sup>10</sup>, critically depend on high- $Q$  resonators. This has led to extensive efforts in

designing ultrahigh- $Q$  resonators across different spectral regimes. However, experimentally realizing very large  $Q$ -factors at shorter wavelengths, e.g., visible wavelengths, remains an outstanding challenge due to material and fabrication constraints. The primary difficulty lies in fabrication imperfections that cause unwanted scattering loss and deviations from the intended design<sup>11–13</sup>, which are much more severe in visible-wavelength devices because their small feature sizes are on a similar scale as fabrication defects.

A full list of affiliations appears at the end of the paper. ✉ e-mail: [jiefang@uw.edu](mailto:jiefang@uw.edu); [arka@uw.edu](mailto:arka@uw.edu)

At visible wavelengths, million-scale ( $10^6$ )  $Q$ -factors have been accessed in individual photonic resonators such as evanescently-coupled micro-ring and micro-disk cavities<sup>1,14</sup>, and free-space-coupled microtoroids<sup>15</sup>. Due to tight spatial confinement of light, one can minimize the defect-sensitive area in these resonators. In contrast, free-space lattice-resonant implementations such as metasurfaces and photonic crystal slabs have larger functional areas (which enable large space-bandwidth product), and thus are highly defect-sensitive and face additional challenges, including long-range non-uniformity, substrate-induced out-of-plane asymmetry, and modal dispersion. Experimentally reported  $Q$ -factors in these free-space resonators typically fall within a scale of only  $10^3$  (see Table 1)<sup>16–21</sup> in the visible regime.

Despite these challenges, there is an outstanding and ever-growing demand for ultrahigh- $Q$  free-space optics due to their distinct advantages of large space-bandwidth product, easy free-space access, and parallel signal/data operations<sup>22,23</sup>. These unmet needs have spurred research into topological metasurfaces that are meticulously engineered to be more resilient to fabrication defects<sup>24–26</sup>, for instance, by merging multiple bound states in the continuum (BICs) in momentum space<sup>24</sup>. However, in these approaches, the substrate needs to be removed to minimize out-of-plane asymmetry and the lack of lossless high-index materials at visible wavelengths may also limit design feasibility. Moreover, despite the improvements, the experimental  $Q$ -factors still fall short by orders of magnitude compared to those in integrated-optics resonators.

Here we design and experimentally demonstrate a million-scale ultrahigh- $Q$  guided mode resonance (GMR) at near-visible wavelengths in a resist-based etch-free metasurface (Fig. 1). Etching is the major process that introduces roughness and defects. An ‘etch-free’ design procedure aims to minimize fabrication imperfections, rather than engineering the device’s robustness to imperfections. The advantage of this novel concept was recently validated by Huang et al. in a near-infrared ultrahigh- $Q$  metasurface<sup>27</sup> and by Ko et al. in a mid-infrared ultrahigh- $Q$  microresonator<sup>28</sup>, among others<sup>29,30</sup>. Expanding on these findings, we adapt the etch-free metasurface strategies<sup>27,29,30</sup> under the material constraints of visible regime, and advance visible-wavelength free space meta-optics into a new era of million- $Q$  performance. We achieve this by using a perturbed multilayer-waveguide configuration as shown in Fig. 1a with material refractive indices not exceeding 2.0 (SiN). We emphasize that low-loss high-index materials are rare at visible wavelengths, and hence our moderate-index design facilitates generalization across different platforms.

To characterize a million- $Q$  resonance under free-space visible wavelength excitations, we develop a new laser-scanning momentum-space-resolved spectroscopy technique. It combines a tunable-wavelength laser and a momentum-space imaging system to visualize the modal dispersion<sup>24,31–34</sup> in the full energy-momentum space with ultrahigh resolution in wavelength ( $\sim 0.42$  pm) and angle ( $\sim 0.028^\circ$ ).

Our platform can be readily used in various applications including optical sensing, filtering, quantum light sources, and few-photon nonlinear optics. As an example, we integrate monolayer WSe<sub>2</sub> into our

ultrahigh- $Q$  meta-optical resonator and demonstrate highly unidirectional and narrow-linewidth exciton emission. The ultrahigh- $Q$  cavity effectively boosts the density of states at the  $\Gamma$  point, and a pump-power-dependent emission concentration towards the  $\Gamma$  point under continuous-wave (CW) laser pumping is observed at room temperature.

## Results

### Design of ultrahigh- $Q$ GMR meta-resonator

The proposed metasurface configuration and the design flow from a nonradiative guided mode to a radiative ultrahigh- $Q$  GMR are illustrated in Fig. 1a, b, respectively. To begin, we consider the four-layer slab waveguide in Fig. 1b, which comprises, from top to bottom, of a semi-infinite air superstrate, a 58-nm-thick layer of polymethyl methacrylate (PMMA), a 100 nm-thick layer of SiN, and a semi-infinite SiO<sub>2</sub> substrate. This stack supports both transverse electric (TE) and transverse magnetic (TM) guided modes with different cut-off wavelengths. For simplicity, we target the wavelengths where only the fundamental TE modes exist (see Supplementary Note 1), for which the electric field is  $E(x, z) = \hat{y}E_y(z)e^{ik_{GM}x}$ .  $k_{GM}$  is the propagation constant (i.e., in-plane component of the guided mode wave vector), which can be found by solving the transcendental dispersion equation (detailed derivation in Supplementary Note 1),

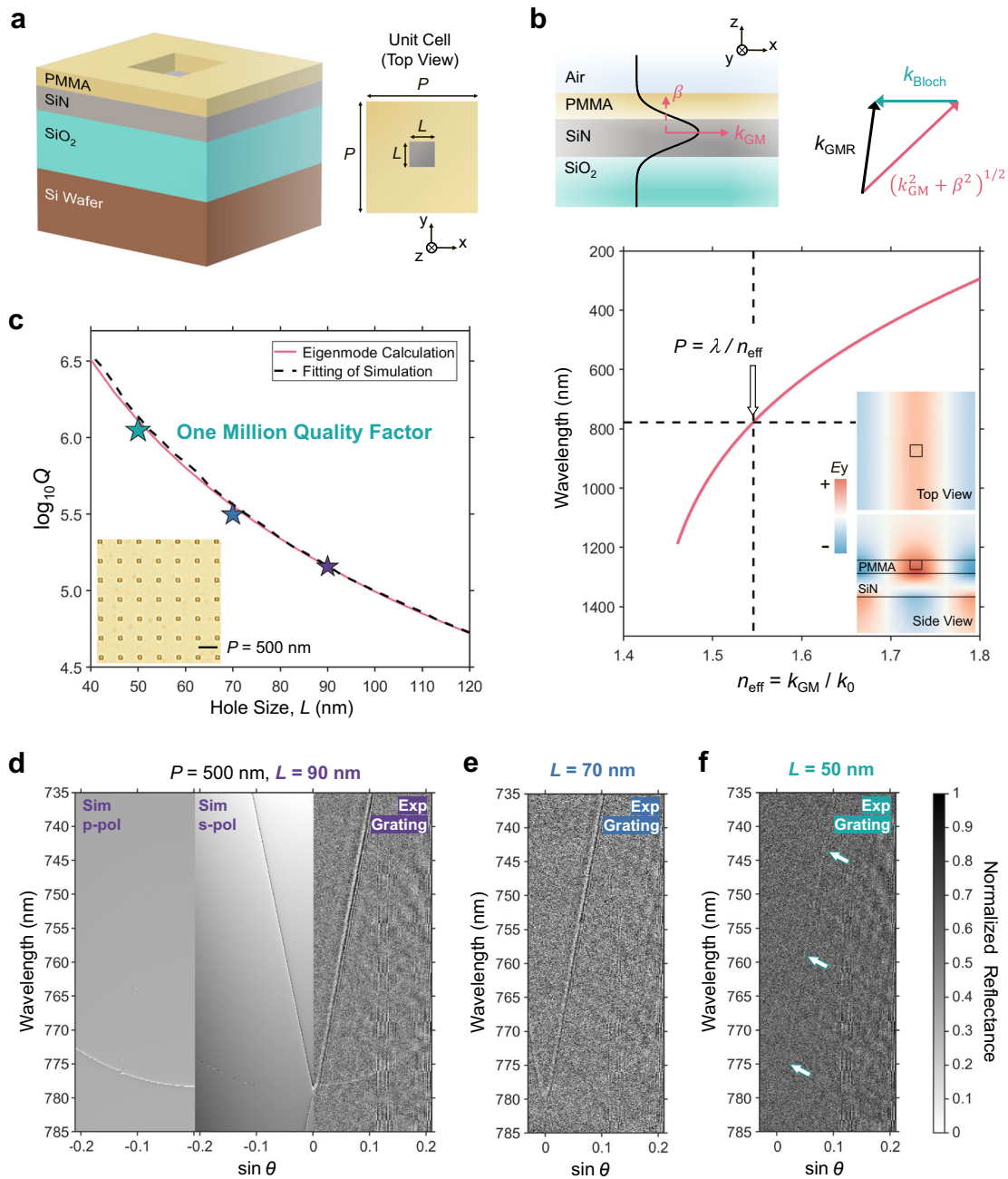
$$\tan \beta_3 h_{SiN} = \frac{\beta_3 (\kappa_1 \kappa_4 - \beta_2^2) \tan(\beta_2 h_{PMMA}) + \beta_3 \beta_2 (\kappa_1 + \kappa_4)}{(\beta_3^2 \kappa_1 + \beta_2^2 \kappa_4) \tan(\beta_2 h_{PMMA}) + \beta_2 (\beta_3^2 - \kappa_1 \kappa_4)} \quad (1)$$

In this equation,  $\beta_2 = [n_{PMMA}^2 k_0^2 - k_{GM}^2]^{1/2}$  and  $\beta_3 = [n_{SiN}^2 k_0^2 - k_{GM}^2]^{1/2}$  are the out-of-plane wave vector components in the PMMA and SiN layers, respectively, where  $k_0 = 2\pi/\lambda$ ;  $\kappa_1 = [k_{GM}^2 - n_{air}^2 k_0^2]^{1/2}$ , and  $\kappa_4 = [k_{GM}^2 - n_{SiO_2}^2 k_0^2]^{1/2}$  are the decay constants in air and SiO<sub>2</sub>, respectively. The symbols  $n$  and  $h$  represent the refractive indices and thicknesses of different media. The plot in Fig. 1b shows the dispersion of the effective index  $n_{eff} = k_{GM} / k_0$  of the TE<sub>1</sub> mode obtained by solving Eq. (1). In Supplementary Fig. S1, we also examine a simplified three-layer model that ignores the very thin resist layer<sup>27</sup>, showing a significant deviation of  $n_{eff}$  compared with the complete four-layer model. This suggests that the very thin PMMA plays a crucial role here, and the optical near field is expected to be effectively trapped in both the SiN and PMMA layers.

By creating a square periodic array of perturbations in the PMMA layer as shown in Fig. 1a, we introduce a structure-induced Bloch momentum  $k_{Bloch} = 2\pi/P$  to compensate for  $k_{GM}$  and thereby open a radiative leaky channel for the infinite- $Q$  guided mode to couple into free space. A wave vector analysis sketch is presented in the top-right panel of Fig. 1b. This leads to a GMR with wave vector  $k_{GMR}$ , whose resonance wavelength is determined by the period of perturbation  $P$  and the guided mode dispersion, as shown in the bottom panel of Fig. 1b. For instance, to design a  $\Gamma$ -point (normal-incidence) GMR at a

**Table 1 | Experimentally reported  $Q$ -factors in free-space optics at visible wavelengths**

Ref.	$Q$	$\lambda$ (nm)	Design / Structure	Device size ( $\mu\text{m}^2$ )
16	8,000	750	GMR / SiO <sub>2</sub> grating on SiN waveguide	10,000 × 15,000
17	391	860	GMR / photoresist grating on HfO <sub>2</sub> waveguide	\
18	32,000	490	GMR / SiN photonic crystal slab	600 × 600
19	10,000	583	Symmetry-protected BIC / SiN photonic crystal slab	7,000 × 7,000
20	2750	825	Symmetry-protected BIC / GaAs metasurface	60 × 108
21	2750	717	Resonance-trapped BIC / TiO <sub>2</sub> lattice on dielectric-covered mirror	500 × 500
This work	<b>1,100,000</b>	<b>779</b>	<b>GMR / patterned PMMA resist on SiN waveguide</b>	<b>900 × 900</b>



**Fig. 1 | Ultrahigh- $Q$  guided mode resonances (GMRs) in an etch-free metasurface at visible wavelengths.** **a** Schematic showing the unit cell of the etch-free metasurface. From top to bottom, the geometry includes a 58 nm-thick patterned PMMA layer, a 100-nm-thick SiN layer, and a 1470 nm-thick SiO<sub>2</sub> layer on a Si substrate. The patterning is defined by the period  $P$  and defect hole size  $L$ . **b** Design principle, from guided modes to ultrahigh- $Q$  GMRs: Top-left, Schematic of an air/58-nm-PMMA/100-nm-SiN/SiO<sub>2</sub> multilayer slab waveguide; Top-right, Wave vector analysis when a periodic perturbation is patterned at the PMMA layer. The Bloch momentum  $k_{\text{Bloch}} = 2\pi/P$  introduced by periodic patterning couples guided modes into free space.  $k_{\text{GM}}$  and  $\beta$  are the in-plane and out-of-plane components of the guided mode wave vector, respectively.  $k_{\text{GMR}}$  is the GMR wave vector; Bottom, Dispersion of the TE<sub>1</sub> guided mode in the studied system, which guides the design of GMR. The dashed black lines show an example of designing a  $\Gamma$ -point resonance at 779 nm. The insets are the corresponding 779 nm GMR mode profiles when  $P = 500$  nm and  $L = 50$  nm. **c**  $Q$ -factor of GMR as a function of  $L$  when  $P$  is fixed as

500 nm. The red curve is predicted by an eigenmode solver in COMSOL Multiphysics®. The dashed black curve comes from the Fano fitting of the simulated reflectance spectra from Lumerical RCWA. The experimental results using the same fitting method are highlighted as three stars, up to one million  $Q$ . The inset is an SEM image of the fabricated metasurface under top view. False colors are added to highlight the patterned PMMA. Scale bar, 500 nm. **d-f** Simulated and experimentally measured momentum-space-resolved reflectance spectra of our meta-resonators. With a fixed  $P$  of 500 nm, devices with different  $L$  are studied: **(d)**  $L = 90$  nm, **(e)**  $L = 70$  nm, **(f)**  $L = 50$  nm. A spectrometer with a 1200-lines/mm grating is used to differentiate the wavelength in spectra. The arrows in **(f)** guide the eyes towards the GMR feature of interest that is vague due to the ultranarrow linewidth beyond the wavelength resolution. A difference operation is performed, subtracting the background (at unpatterned-PMMA areas) signals from the device signals, to eliminate the multilayer interference influence. The spectra are normalized to their respective maxima (see Methods).

given wavelength  $\lambda$ , we need a  $k_{\text{GMR}}$  with zero in-plane component,  $n_{\text{eff}} \cdot \frac{2\pi}{\lambda} - \frac{2\pi}{P} = 0$ . The dashed lines in the dispersion plot give an example of determining the value of  $P$  for a resonance at 779 nm. Moreover, with a fixed  $P$ , we can use the guided mode dispersion curve to predict the GMR dispersion (Supplementary Fig. S2). The inset shows the simulated mode profiles of a 779 nm resonance at the  $\Gamma$  point when  $P = 500$  nm and the defect hole size  $L = 50$  nm. From the side view, the resonant near field is clearly trapped at the interface of SiN and PMMA, as predicted by the four-layer model. This feature can guide the design strategy to maximize the field overlap with the integrated functional materials, which will be further discussed in the last section.

Similar to a quasi-BIC leaky mode<sup>26,35</sup>, the extent of periodic perturbations (hole size) applied on a photonic bound state (nonradiative guided mode) determines the  $Q$ -factor and radiative amplitude of the leaky mode (GMR)<sup>27</sup>. In our metasurface, a smaller  $L$  induces a larger  $Q$ -factor as shown in Fig. 1c, accompanied by a decreased reflectivity amplitude as shown in Supplementary Fig. S3 (the amplitude decrease is negligible for the hole sizes chosen in our experimental demonstration). The predicted  $Q$ -factors in Fig. 1c are obtained through eigenmode simulations (red solid line) and Fano fitting of simulated reflection data (black dashed line). The close agreement between these methods validates the fitting approach, which is then applied to all experimental spectra (see Methods).

Three metasurfaces with fixed  $P = 500$  nm and varying  $L$  (90, 70, 50 nm) are fabricated and characterized. Note that, to ease the fabrication without affecting the design (Supplementary Fig. S4), the samples are fabricated on 1470 nm-SiO<sub>2</sub>-on-Si wafers as illustrated in Fig. 1a. The  $Q$ -factors of these three devices (stars in Fig. 1c) all show excellent agreement with the theoretical expectation, yielding a record-high  $Q$  of a million scale. Such good quantitative agreement is thanks to the reduced amount of fabrication imperfection enabled by the etch-free design, where only the PMMA layer is patterned by electron-beam lithography and a development process, eliminating the need for etching.

### Visualization of GMR dispersions

Random device defects, environmental noise, light path misalignment, or even dust on optical components can cause ‘ghost’ narrow-linewidth spectral features in visible-wavelength free-space measurements. When the linewidth of the studied resonance mode is comparable to these high-frequency background signals, experimental spectral analysis becomes less convincing. To properly characterize an ultrahigh- $Q$  meta-resonator, we need momentum-space-resolved spectroscopy that enables the visualization of the complete modal dispersions, thereby distinguishing the real resonances from various noise sources<sup>24,32,34</sup>. Here, we start with a conventional energy-momentum reflectance spectroscopy that uses a white light source and a grating (see the optical setup in our previous publications<sup>36,37</sup>). As shown in Fig. 1d–f, the measured dispersion of all three devices matches well with the simulated GMR response in Fig. 1d, confirming the GMR nature of the measured high- $Q$  modes and again proving the near-ideal performance of our etch-free metasurfaces. Figure 1d also reveals the co-existence of different resonance modes with s- or p-polarization. A full eigenmode analysis can be found in Supplementary Note 2. In the main text, we focus on the s-polarized ultrahigh- $Q$  GMR with a clean linear dispersion, as highlighted by the arrows in Fig. 1f.

We find that, as the  $Q$ -factor increases with decreasing  $L$  (from Fig. 1d–f), the ultrahigh- $Q$  GMR dispersion curve becomes faint. This suggests that the linewidth of the studied resonance mode is much smaller than the wavelength resolution ( $\sim 0.05$  nm) of the 1200-lines/mm grating in the setup. Since interference-induced high- $Q$  resonances typically manifest as an asymmetric Fano shape with one peak and one dip, insufficient wavelength resolution can average out the peak and dip, causing incorrect or missing spectral information.

To tackle this intriguing dilemma arising from a record-high  $Q$  in visible-wavelength free-space optics—a unique and new task that could become common as our strategy can be easily generalized—we introduce a laser-scanning momentum-space-resolved spectroscopy technique, as shown in Fig. 2a. Analogous to integrated photonic resonator measurements, a tunable laser is employed to scan the wavelength with extremely high resolution. Distinctively, the wavelength-scanning laser is integrated into a 4- $f$  momentum-space imaging system, and a two-dimensional charge-coupled device (2D CCD) continuously captures the iso-frequency contours of the photonic band structures at different wavelengths determined by the tunable laser.

With full access to the multi-dimensional information in the wavelength/energy-momentum ( $E$ - $k$ ) space, we can visualize any  $E$ - $k$  cross-section, such as a cut along  $\hat{k}_y$  in Fig. 2b–d. In most cases, we enable a small number of pixels on the 2D CCD, only collecting the desired  $E$ - $k$  information, to save scanning time. See Methods and Supplementary Note 3 for technique details. As an aside, we target the 779-nm GMR designs for our experimental demonstrations because the only accessible tunable laser in our lab covers 765 to 781 nm. Devices working at shorter wavelengths have also been fabricated and studied (Supplementary Fig. S5). Ultrahigh-resolution quantitative characterization can readily be performed using the same method as long as a tunable laser is available at the relevant wavelength.

Figure 2b–d compare the results of conventional energy-momentum reflectance spectroscopy with our laser-scanning-integrated approach. Measured spectra from the metasurface with  $P = 500$  nm and  $L = 90$  nm are presented as an example. Dramatic improvements can be found in Fig. 2c, d (laser-scanning) compared to Fig. 2b (conventional), successfully detecting the ultrahigh- $Q$  spectral feature in visible-wavelength free-space measurements.

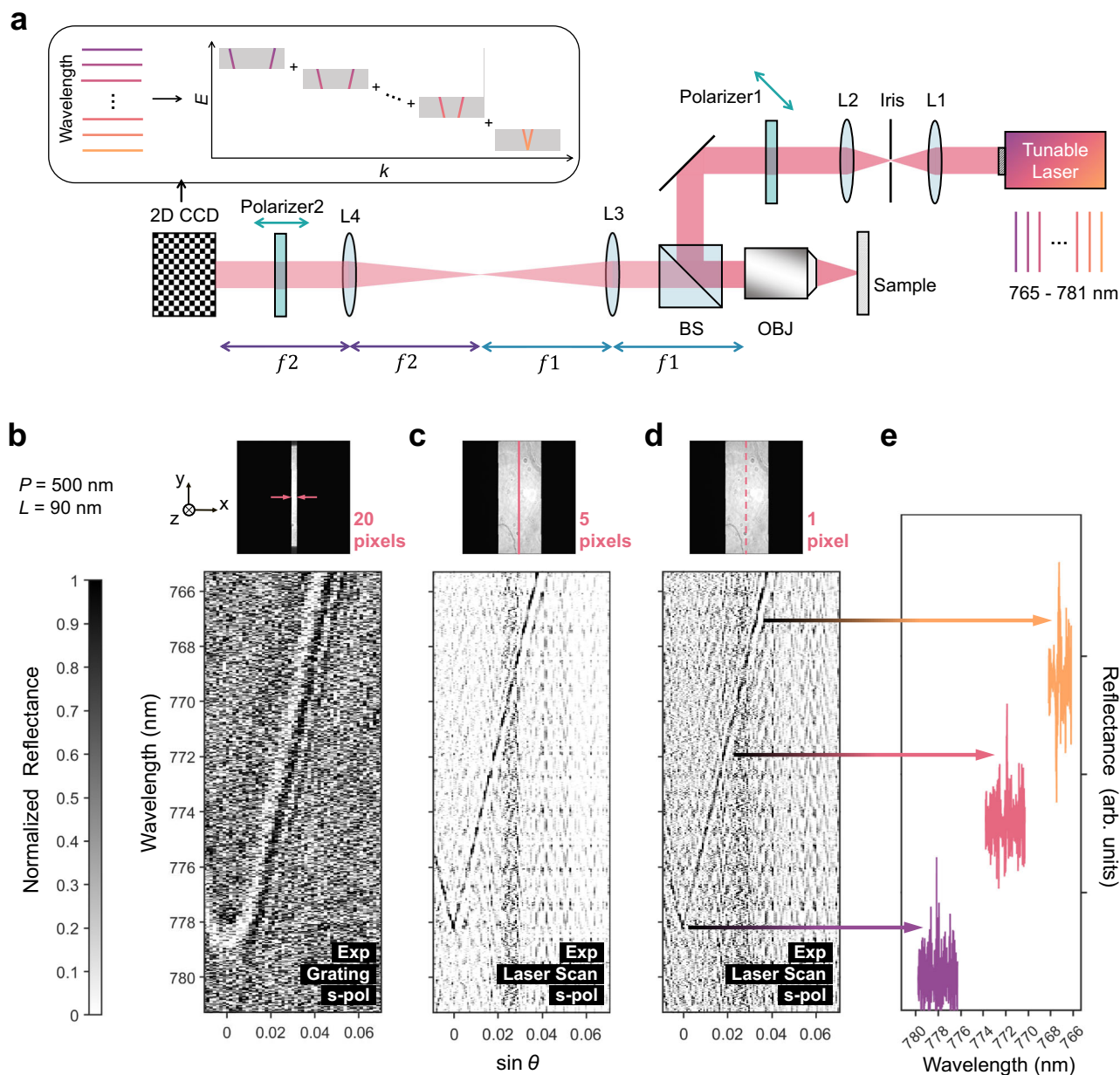
Besides improving the resolution in wavelength and momentum (angle), we also examine the influence of the number of pixels summed along the direction perpendicular to the visualized  $E$ - $k$  cross-section (e.g.,  $\Delta k_x$  in  $\mathbf{X}$  axis for a  $E$ - $k$  cross-section cut along the  $\mathbf{Y}$  axis). In common spectroscopy approaches using gratings, a slit must be applied as shown in the top inset of Fig. 2b. The slit width needs to balance the grating efficiency and resolution, and the optimal width in our setup turns out to be at least 20 pixels wide. This causes extra dispersion-induced mode broadening<sup>37</sup>. Excitingly, our technique allows to sum an arbitrary number of pixels, as illustrated in the top insets of Fig. 2c, d. With more pixels summed (Fig. 2c), the signal-to-background ratio is higher, while the single pixel case (Fig. 2d) can provide the narrowest GMR feature, closer to the intrinsic GMR property. In the following, we display the  $E$ - $k$  spectra with a few pixels summed and extract  $Q$ -factors from single-pixel data.

### Direct measurement of a million $Q$

With sufficient resolutions in  $E$ - $k$  space and a clear GMR dispersion picture, we can extract high-wavelength-resolution 1D spectra at arbitrary  $k$  values and confidently identify the high- $Q$  peaks originating from the GMR meta-resonator, as shown in Fig. 2e.

Based on this, we fit a Fano lineshape to the extracted 1D spectra at the  $\Gamma$  point ( $k = 0$ ), highlighted by the arrow in the right panel of Fig. 3a) and determine the  $Q$ -factors of three fabricated metasurfaces to be  $1.10 \pm 0.09$  million ( $L = 50$  nm, Fig. 3a),  $313 \pm 8$  thousand ( $L = 70$  nm, Fig. 3b), and  $144 \pm 5$  thousand ( $L = 90$  nm, Fig. 3c), respectively. As concluded in Table 1, our report of a million  $Q$  in the experiment is orders of magnitude higher than state-of-the-art demonstrations in visible-wavelength free space meta-optics<sup>16–21</sup>.

Looking beyond the million- $Q$  achievements, further advancements will require a faster 2D camera and a more stable tunable laser. Here, to obtain enough data points for accurately fitting a million- $Q$  resonance, we reduce the laser scanning speed while the 2D CCD capture frequency is already at its maximum, achieving a wavelength resolution as fine as  $\sim 0.42$  pm. However, as shown in the right panel of



**Fig. 2 | Laser-scanning momentum-space-resolved spectroscopy with ultrahigh resolutions in wavelength and angle of signal.** **a** Schematic of the optical setup and how laser-scanning defines wavelength in momentum-space-resolved spectroscopy. L1-4, lens. BS, beamsplitter. OBJ, objective. CCD, charged-coupled device camera. More details in optical setup and measurements can be found in Methods. **b-d** Comparison of the measured momentum-space-resolved reflectance spectra under different wavelength and angle resolutions. Spectra of the device with  $P = 500$  nm and  $L = 90$  nm are presented as an example. A spectrometer with a

1200-lines/mm grating provides a wavelength resolution of  $\sim 0.05$  nm/pixel in **(b)**, while a resolution of  $\sim 2.1$  pm/pixel is achieved in **(c, d)** via a tunable laser. The angle resolution is  $\sim 0.076^\circ$ /pixel in **(b)** with a 10X objective, and  $\sim 0.044^\circ$ /pixel in **(c, d)** with a 2X objective. Insets on top highlight the numbers of pixels summed along  $X$  axis on CCD when evaluating the momentum-dependent spectral response along  $Y$  axis. The more pixels summed, the more severe the dispersion-induced mode broadening is. **e** Reflectance spectra extracted at arbitrary  $k$  values in the momentum space from **(d)**.

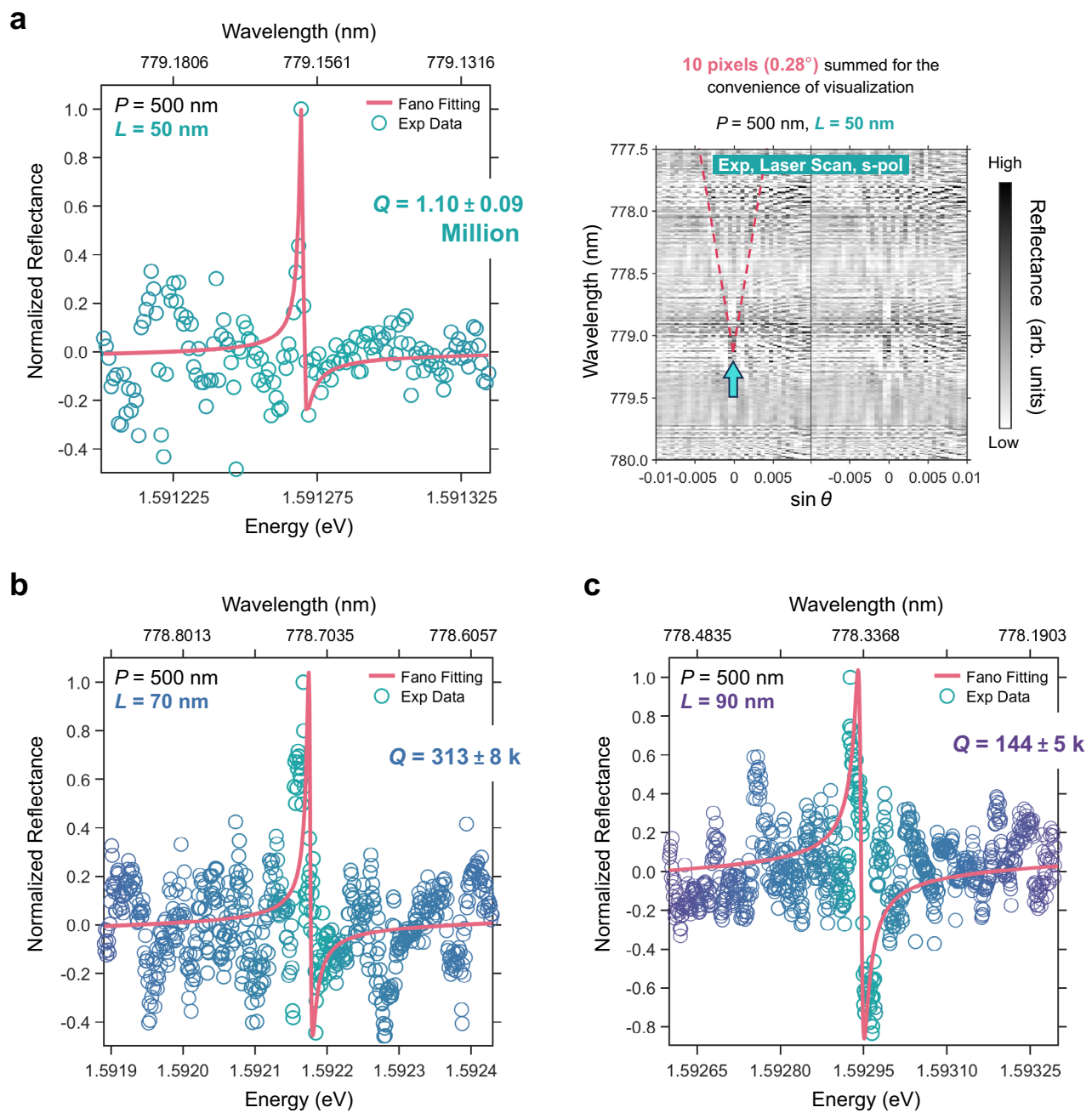
Fig. 3a, an unwanted stripe-like background emerges in this extra-fine momentum-space-resolved spectrum, resulting from laser instability over the longer scanning time.

#### A unidirectional and narrow-linewidth exciton emitter

In this last section, we demonstrate the practical advantages of our ultrahigh-Q meta-optical platform by integrating monolayer WSe<sub>2</sub> into the metasurface and showcasing a highly unidirectional and narrow-linewidth exciton emitter at room temperature beyond the intrinsic material limitation. Monolayer transition metal dichalcogenides (TMDs) such as WSe<sub>2</sub> are promising next-generation nano-emitters but suffer from poor emission directionality<sup>38</sup> and broad spectral linewidth

at room temperature<sup>39</sup>. As shown in the left part of Fig. 4a (white-to-purple colormap), the room temperature photoluminescence (PL) of a monolayer WSe<sub>2</sub> (under a 532 nm CW laser pumping) in our unpatterned multilayer structure has a full-width-at-half-maximum (FWHM) spectral linewidth ( $\Gamma_\lambda$ ) of  $\sim 25.12$  nm and shows very poor directivity with a FWHM linewidth in far-field emission angle ( $\Gamma_\theta$ ) of  $\sim 120.95^\circ$  (see simulated 3D emission directionality in Supplementary Fig. S6). Our ultrahigh-Q platform can substantially narrow both of these important figures of merit by more than 96% (Fig. 4b).

As shown in the right part of Fig. 4a (grayscale), we select a metasurface period  $P$  of 480 nm to match the  $\Gamma$  point of GMR with the WSe<sub>2</sub> PL in wavelength. A defect hole size  $L$  of 70 nm is used, yielding a



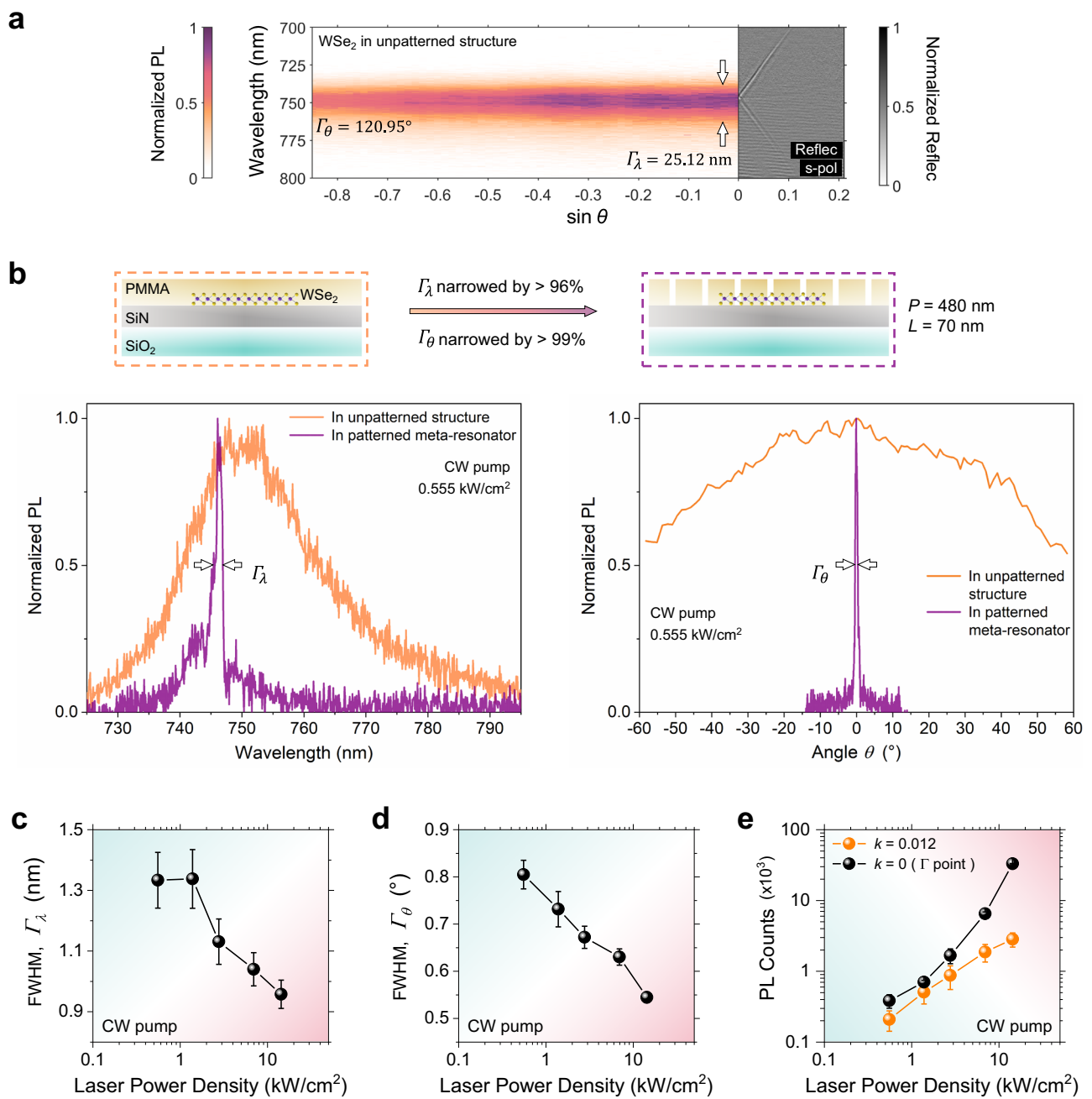
**Fig. 3 | Experimental demonstration of million-Q GMR at near-visible wavelengths.** **a** Left, Reflectance spectra of the device with  $P = 500$  nm and  $L = 50$  nm at  $\Gamma$  point (normal incidence). The Fano fitting (pink curve) reveals a  $Q$  factor of 1.10 million. The  $\Gamma$ -point data are extracted from extra-fine laser-scanning momentum-space-resolved reflectance spectroscopy with a wavelength resolution of  $-0.42$  pm/pixel and an angle resolution of  $-0.028^\circ$ /pixel; Right, the momentum-space-resolved spectra where the  $\Gamma$ -point data is extracted from. Note that a  $0.28^\circ$

range (10 pixels) of data are summed to broaden the ultranarrow mode linewidth for the convenience of visualization here, but only single-pixel data are used for Fano fittings. The same momentum-space-resolved spectra are plotted twice, one with the pink dashed lines highlighting the dispersion of GMR. The arrow points to the  $\Gamma$ -point resonance. **b**, **c** The same as **(a)** but for the devices with **(b)**  $L = 70$  nm and **(c)**  $L = 90$  nm. The fitted  $Q$  factors are 313 and 144 thousand respectively.

$Q$ -factor of  $\sim 297$  thousand, which is still higher than any reported  $Q$  in literatures<sup>16–21</sup>. As illustrated in Fig. 4b, monolayer  $\text{WSe}_2$  is placed between SiN and PMMA layers for better field overlap (see the mode profile inset in Fig. 1b). This is easily achieved by first transferring the functional material, i.e., exfoliated  $\text{WSe}_2$ , onto SiN and then performing the spin coating and lithography in PMMA.

The  $\text{WSe}_2$  PL linewidths in the unpatterned structure and patterned ultrahigh- $Q$  meta-resonator are compared in Fig. 4b, in both spectral (left panel) and angular (right panel) dimensions, showing

laser-like monochromaticity and unidirectionality when coupled with the metasurface at room temperature, albeit without any operating power density threshold. The applied CW pumping power density is as low as  $0.555$  kW/cm<sup>2</sup>. The spectral and angular plots in Fig. 4b are extracted from the energy-momentum PL spectra of the  $\text{WSe}_2$ -metasurface hybrid in Supplementary Fig. S7, which reveal the highly concentrated emission at the  $\Gamma$  point of GMR. Such achievement enables the practical applications of 2D TMD materials in displays and optical communications. We emphasize that, compared to the 2D material



**Fig. 4 | Highly unidirectional and narrow-linewidth exciton emission from monolayer WSe<sub>2</sub> when coupled with the ultrahigh-Q meta-resonator at room temperature.** **a** Left, Energy-momentum photoluminescence (PL) spectra of monolayer WSe<sub>2</sub> in the unpatterned structure. Pumped by a 532 nm 0.555 kW/cm<sup>2</sup> CW laser. The broad full-width-at-half-maximum (FWHM) linewidths in far-field emission angle ( $\Gamma_\theta$ ) and spectral wavelength ( $\Gamma_\lambda$ ) are highlighted; Right, Energy-momentum reflectance spectra of the WSe<sub>2</sub>-metasurface hybrid system, where  $P = 480$  nm and  $L = 70$  nm. **b** Narrowing the WSe<sub>2</sub> PL in both spectral and angular dimensions. Top, Schematics of monolayer WSe<sub>2</sub> in the unpatterned structure and patterned meta-resonator on a fused silica substrate (no Si wafer), respectively. The

same device is measured before and after PMMA patterning. Bottom, Comparison of WSe<sub>2</sub> PL linewidths before and after patterning, in both spectral (Left) and angular (Right) dimensions. **c–e** Extracted emission properties of the WSe<sub>2</sub>-meta-surface hybrid from the energy-momentum PL spectra (Supplementary Fig. S7) as a function of pump power density (logarithmic scale): **(c)** spectral linewidth, FWHM  $\Gamma_\lambda$ , **(d)** angular linewidth, FWHM  $\Gamma_\theta$ , and **(e)** integrated PL counts (logarithmic scale) at  $\sin \theta = 0.012$  (orange dots) and  $\sin \theta = 0$  ( $\Gamma$  point) (black dots), respectively. The error bars in **(c, d)** are determined by spectra fittings (see Methods). The integrated PL in **(e)** were measured by first increasing the laser power and then decreasing it by 3 times. The error bar shows the standard deviation.

integration with nanostructured cavities, our approach of sandwiching TMDs between two thin layers can be well extended to large-scale integration with chemical vapor deposition (CVD)-grown layered materials.

Additionally, as we increase the 532 nm pump power density, we observe obvious PL narrowing in both spectral ( $\Gamma_\lambda$ ) and angular ( $\Gamma_\theta$ ) dimensions. A power-dependent analysis is performed, and the

extracted crucial parameters are presented in Fig. 4c–e. It should be emphasized that the heating effect is carefully excluded in our CW laser pumping tests. Referring to a literature<sup>40</sup> that studied 532 nm laser-induced heating on WSe<sub>2</sub> (the same laser wavelength and material) with rigorous experiments and simulations, we set our CW laser power density to a safe range where no detectable temperature increase was found<sup>40</sup>.

As shown in Fig. 4c, d, the FWHM  $\Gamma_\lambda$  is narrowed from 1.334 nm to 0.957 nm (by -28%), and FWHM  $\Gamma_\theta$  is narrowed from 0.805° to 0.545° (by -32%) under 14.33 kW/cm<sup>2</sup> CW pumping. To better understand this narrowing phenomenon, in Fig. 4e, we examine the integrated PL counts at  $\Gamma$  point ( $k=0$ ) and at  $k=0.012$ , slightly deviated from the  $\Gamma$  point, as a function of pump power density. We choose a very small deviation from the  $\Gamma$  point because the emission is already well concentrated even before we increase the pump power and PL signals at larger  $k$  values are near zero. As shown in Fig. 4e, a nonlinear increase of PL counts at  $k=0$  is found, while there is a saturation trend in term of PL counts at  $k=0.012$ , suggesting amplified spontaneous emission (ASE) in our system because of the extremely high density of state at the  $\Gamma$  point thanks to the record-high  $Q$ -factors.

We have also conducted PL studies at higher power densities by using a 532 nm 100-picosecond pulsed laser and a consistent power-dependent narrowing tendency is found (Supplementary Fig. S8), further supporting the ASE assumption. The narrowed FWHM  $\Gamma_\lambda$  and  $\Gamma_\theta$  eventually saturate at 0.587 nm and 0.269° under pulsed pumping. More discussions can be found in Supplementary Note 4.

Lastly, we notice strong in-plane scattering at the boundaries of the finite-size WSe<sub>2</sub> flake (see Supplementary Note 4 and Figs. S7, S10), possibly because of the significant refractive index difference between WSe<sub>2</sub> ( $n > 4.4$ ) and our multilayer waveguide structure ( $n < 2.0$ ). Consequently, we hypothesize that both the strong temporal confinement of our ultrahigh- $Q$  GMR and the considerable spatial confinement due to the high-index WSe<sub>2</sub> monolayer disk (acting like an in-plane resonator) contribute to the observed extreme emission concentration at RT and under CW pumping. Further studies are inspired but beyond the scope of this work.

## Discussion

In conclusion, we have experimentally demonstrated a record-high million-scale ultrahigh- $Q$  GMR at near-visible wavelengths under free-space excitation using an etch-free metasurface. Advancing free space meta-optics into a new era of million- $Q$  performance, we have also developed a laser-scanning momentum-space-resolved spectroscopy technique to accurately characterize arbitrary dispersive ultrahigh- $Q$  modes in the challenging free-space optical measurements. With material refractive indices not exceeding 2.0 in the demonstrated million- $Q$  device and the simple resist-based fabrication procedure, our strategy can be easily generalized across various platforms at visible wavelengths, inspiring more complicated meta-resonator designs (chiral<sup>41</sup>, topological<sup>24–27</sup>, nonreciprocal<sup>42</sup>, reconfigurable<sup>43</sup>, etc.) and functional material integration.

Furthermore, we have integrated monolayer WSe<sub>2</sub> into our ultrahigh- $Q$  meta-optical resonator and demonstrated a highly unidirectional and narrow-linewidth exciton emitter operating at RT and under CW pumping. Extreme PL concentration with FWHM linewidths as narrow as 0.269° in far-field emission angle and 0.587 nm in wavelength has been achieved, offering a laser-like light source without any power density threshold requirement. Pump-power-dependent linewidth narrowing and nonlinear increase in PL counts are observed, suggesting ASE in our system and highlighting the potential of our ultrahigh- $Q$  meta-optics platform for studying cavity-modulated quantum emitters and low-photon-number nonlinear optics. Additionally, our result holds great promise for applications like optical sensing, filtering, and metrology.

## Methods

### Metasurface fabrication

All metasurfaces without WSe<sub>2</sub> emitter integration (Figs. 1–3 and Supplementary Fig. S5) are fabricated on a 1470 nm-thick SiO<sub>2</sub> on silicon substrate (UniversityWafer, Inc.). The device for WSe<sub>2</sub> integration and PL measurements (Fig. 4) is fabricated on a JGSI fused silica substrate (UniversityWafer, Inc.). A 100 nm-thick layer of Si<sub>3</sub>N<sub>4</sub> is grown on top of the substrates through low-pressure chemical vapor deposition

(LPCVD) by UniversityWafer, Inc. The wafer is then diced into 8×8 mm<sup>2</sup> chips (DAD321, Disco America).

The chips are thoroughly cleaned by sonication in acetone, followed by isopropyl alcohol (IPA), each for 5 min. After that, the SiN surface is treated by oxygen plasma at 150 W for 5 min to dry the surface and remove any solvent residue (AutoGlow, Glow Research). Subsequently, a 58 nm-thick layer of positive-tone resist PMMA is spin-coated and annealed under 180 °C for 3 min. After cooling the chip to room temperature, a layer of conductive polymer (DisCharge H<sub>2</sub>O) is spin-coated on top. The metasurface pattern is defined using a JEOLJXB-6300FS 100 kV electron-beam lithography system, followed by development in a cold water/IPA mixture for 2 min. The fabrication is etch-less, ensuring minimized sidewall roughness of the patterns.

### Preparation of monolayer WSe<sub>2</sub>

WSe<sub>2</sub> flakes are directly transferred onto the SiN surface using the standard tape exfoliation method. Monolayers are identified by checking the imaging contrast under optical microscope and confirmed using atomic force microscopy (AFM).

### Optical setup and measurement

Optical characterizations are performed using a custom-built optical setup (Fig. 2a). Light is introduced into the setup via a single-mode fiber. The tunable laser (Newport TLB-6712), continuous-wave pump (Laserglow Technologies 532 nm DPSS Laser), and pulsed pump (NKT SuperK FIU-15 Laser, 78 MHz repetition rate, with a SuperK SELECT tunable multi-channel filter) are all coupled in this manner. The light is first focused on a 75 μm iris using L1 (focal length,  $f=60$  mm) and L2 ( $f=75$  mm) to ensure a uniform Gaussian beam. An objective lens is used to both focus the light onto the sample and collect the reflection/PL signals. To obtain the momentum-space-resolved spectrum, a telescope consisting of lenses L3 ( $f=180$  mm) and L4 ( $f=150$  mm) is employed. Here, L3 and L4 are confocal, L3 is in focus with the back focal plane of the objective lens, and L4 is in focus with the spectrometer CCD (Princeton Instruments Isoplan 160 with PIXIS 400).

In the laser-scanning momentum-space-resolved reflectance measurements (Fig. 2c, d and Fig. 3), a 2X Mitutoyo Plan Apo Infinity Corrected Long WD Objective (numerical aperture, NA 0.055) is used. To improve the signal-to-noise ratio, a crossed-polarization measurement method<sup>24,27</sup> (Supplementary Note 3) is employed by inserting two linear polarizers into the excitation and collection light paths, respectively, as shown in Fig. 2a. The second polarizer also determines the polarization of the GMR modes. Note that there is no mirror between Polarizer1 and BS in the actual setup, and a plate beamsplitter is used instead of a cube beamsplitter to avoid extra interference caused by reflections at the optical interfaces. For signal collection, we use the 2D CCD in the commercial spectrometer with the grating disabled. The wavelength scanning of the tunable laser and the data capture by the CCD are synchronized and controlled by a Python script.

In the PL measurements (Fig. 4), a 10X Olympus PLN Objective (NA 0.25) is used. With a 650 nm short-pass filter in the excitation pathway and a 550 nm long-pass filter in the collection pathway, we filter the pump laser and ensure a clean PL signal. A single linear polarizer is inserted into the collection light path to ensure a clean s-polarized GMR signal. For signal collection, we use the commercial spectrometer with the 1200-lines/mm grating enabled.

### Spectroscopy data processing

In the reflectance measurements (Figs. 1, 2, 3), both the device and background (the unpatterned-PMMA areas next to the device) spectra are collected –  $R_{\text{device}}$  and  $R_{\text{BG}}$ . First, a difference operation is performed,  $R_0 = R_{\text{device}} - R_{\text{BG}}$ , to eliminate the multilayer interference influence. Then, low-frequency noise signals are filtered, as our ultrahigh- $Q$  GMR signal is super high-frequency. The noise involves light source fluctuation, photodetector background, and the interference



introduced by optical components like beamsplitters and lenses (the interference is severe when a tunable laser with good coherence is applied). The noise filtering is achieved via a customized two-dimensional bandpass filter in MATLAB, which transforms the data to the Fourier space by fast Fourier transform and selects the frequency components within an anisotropic elliptical donut-shaped region. The cutoff frequency is carefully chosen such that only the relatively low-frequency noise is filtered without affecting the high- $Q$  signal. A linearly gradual cutoff is implemented to mitigate the ‘ring’ artifact due to abrupt frequency cutoff. The code is available on: <https://github.com/charey6/2D-frequency-filter.git>. Finally, the spectra are normalized to their respective maxima.

In the PL measurements (Fig. 4), after subtracting the setup background signals, the measured spectra are directly normalized to their respective maxima.

### Spectra fittings

Spectra fittings are performed using a commercial software MagicPlot. For the spectra fittings in Fig. 3, the Fano fitting equation<sup>44</sup> below is manually written into the software:

$$R_{\text{Fano}}(\lambda) = a \left[ \frac{(b + 2(\lambda - \lambda_0)/\Gamma)^2}{1 + (2(\lambda - \lambda_0)/\Gamma)^2} c + (1 - c) \right]$$

where  $R_{\text{Fano}}$  is the spectrum to be fitted.  $a$ ,  $b$ ,  $c$  are constant real numbers.  $\Gamma$  and  $\lambda_0$  are the resonance FWHM linewidth and center wavelength. The  $Q$ -factor is then determined by  $Q = \lambda_0/\Gamma$ .

For the linewidth fittings in Fig. 4c, d, the Gaussian equation below is used:

$$PL(X) = A \cdot e^{-\ln(2) \frac{(X - X_0)^2}{\Gamma^2}}$$

where  $PL(X)$  is the spectrum to be fitted.  $X$  can be the wavelength or momentum (angle).  $A$  is a constant real number.  $\Gamma$  is the FWHM linewidth in wavelength or momentum (angle), and  $X_0$  is the center wavelength or zero angle (normal incidence).

The fitting errors are evaluated through the residual standard deviations automatically generated by the software in the fitting process. In specific, the software uses iterative Levenberg-Marquardt nonlinear least squares curve fitting algorithm to find the minimum residual sum of squares. Then, the corresponding residual standard deviation is used to describe the root mean square of the error (over all the data points) for the fitted parameters.

### Numerical simulations

The commercial software Ansys Lumerical is used to simulate the momentum-space-resolved reflectance spectra of the metasurfaces (Fig. 1d) using rigorous coupled-wave analysis method (RCWA). As confirmed by ellipsometry (J.A. Woollam M-2000), we consider a 58 nm-thick PMMA with a refractive index of 1.46, a 100 nm-thick SiN with a refractive index of 1.99, and a 1470 nm-thick SiO<sub>2</sub> with a refractive index of 1.44. Based on SEM measurements (Thermo Fisher Scientific Apreo 1), a slightly deviated device period  $P$  of 504 nm is applied. The SEM images can be found in Supplementary Fig. S11. Additionally, through AFM (Bruker Dimension Icon), we find that the defect hole depth is only ~40 nm, not completely penetrating the PMMA layer. This factor is also considered in the simulations.

Eigenmode analyses are conducted using a commercial finite element method solver, the wave optics module in COMSOL Multiphysics® 5.2 and 6.0. For each valid complex eigenfrequency  $f = \Omega + i\Gamma/2$  found, where  $\Omega$  and  $\Gamma$  are respectively the resonance frequency and damping rate, the  $Q$ -factor is determined by  $Q = \Omega/\Gamma$ .

### Data availability

All relevant data that support the findings are available within this Article and Supplementary Information. Source data are available from the corresponding authors upon request.

### Code availability

The bandpass-filter code is available on: <https://github.com/charey6/2D-frequency-filter.git>.

### References

- Lukin, D. M., Guidry, M. A. & Vučković, J. Integrated quantum photonics with silicon carbide: challenges and prospects. *PRX Quantum* **1**, 020102 (2020).
- Solntsev, A. S., Agarwal, G. S. & Kivshar, Y. S. Metasurfaces for quantum photonics. *Nat. Photonics* **15**, 327–336 (2021).
- Wang, M. et al. Suppressing material loss in the visible and near-infrared range for functional nanophotonics using bandgap engineering. *Nat. Commun.* **11**, 5055 (2020).
- Kippenberg, T. J., Holzwarth, R. & Diddams, S. A. Microresonator-based optical frequency combs. *Science* **332**, 555–559 (2011).
- Chang, L., Liu, S. & Bowers, J. E. Integrated optical frequency comb technologies. *Nat. Photonics* **16**, 95–108 (2022).
- Pavlov, N. G. et al. Narrow-linewidth lasing and soliton kerr microcombs with ordinary laser diodes. *Nat. Photonics* **12**, 694–698 (2018).
- He, L., Özdemir, Ş. K. & Yang, L. Whispering gallery microcavity lasers. *Laser Photonics Rev.* **7**, 60–82 (2013).
- Hwang, M.-S., Jeong, K.-Y., So, J.-P., Kim, K.-H. & Park, H.-G. Nanophotonic nonlinear and laser devices exploiting bound states in the continuum. *Commun. Phys.* **5**, 1–12 (2022).
- Vaskin, A., Kolkowski, R., Koenderink, A. F. & Staude, I. Light-emitting metasurfaces. *Nanophotonics* **8**, 1151–1198 (2019).
- Mabuchi, H. & Doherty, A. C. Cavity quantum electrodynamics: coherence in context. *Science* **298**, 1372–1377 (2002).
- Wang, J., Zhan, T., Huang, G., Chu, P. K. & Mei, Y. Optical microcavities with tubular geometry: properties and applications. *Laser Photonics Rev.* **8**, 521–547 (2014).
- Kühne, J. et al. Fabrication robustness in BIC metasurfaces. *Nanophotonics* **10**, 4305–4312 (2021).
- Yang, H. et al. Effects of roughness and resonant-mode engineering in all-dielectric metasurfaces. *Nanophotonics* **9**, 1401–1410 (2020).
- Ji, X., Roberts, S., Corato-Zanarella, M. & Lipson, M. Methods to achieve ultra-high quality factor silicon nitride resonators. *APL Photonics* **6**, 071101 (2021).
- Suebka, S., McLeod, E. & Su, J. Ultra-high- $Q$  free-space coupling to microtoroid resonators. *Light Sci. Appl.* **13**, 75 (2024).
- Zhou, Y. et al. High- $Q$  guided mode resonance sensors based on shallow sub-wavelength grating structures. *Nanotechnology* **31**, 325501 (2020).
- Liu, Z. S., Tibuleac, S., Shin, D., Young, P. P. & Magnusson, R. High-efficiency guided-mode resonance filter. *Opt. Lett.* **23**, 1556–1558 (1998).
- Lee, J., Zhen, B., Chua, S.-L., Shapira, O. & Soljačić, M. Fabricating centimeter-scale high quality factor two-dimensional periodic photonic crystal slabs. *Opt. Express* **22**, 3724–3731 (2014).
- Lee, J. et al. Observation and differentiation of unique high- $Q$  optical resonances near zero wave vector in macroscopic photonic crystal slabs. *Phys. Rev. Lett.* **109**, 067401 (2012).
- Ha, S. T. et al. Directional lasing in resonant semiconductor nanoantenna arrays. *Nat. Nanotechnol.* **13**, 1042–1047 (2018).
- Zhao, G. et al. Unidirectional lasing from mirror-coupled dielectric lattices. *Nano Lett.* **24**, 3378–3385 (2024).

22. Kuznetsov, A. I. et al. Roadmap for optical metasurfaces. *ACS Photonics* **11**, 816–865 (2024).
  23. Hu, J. et al. Diffractive optical computing in free space. *Nat. Commun.* **15**, 1525 (2024).
  24. Jin, J. et al. Topologically enabled ultrahigh-Q guided resonances robust to out-of-plane scattering. *Nature* **574**, 501–504 (2019).
  25. You, J. W. et al. Topological metasurface: from passive toward active and beyond. *Photonics Res.* **11**, B65–B102 (2023).
  26. Bulgakov, E. N. & Maksimov, D. N. Topological bound states in the continuum in arrays of dielectric spheres. *Phys. Rev. Lett.* **118**, 267401 (2017).
  27. Huang, L. et al. Ultrahigh-Q guided mode resonances in an all-dielectric metasurface. *Nat. Commun.* **14**, 3433 (2023).
  28. Ko, K. et al. A mid-infrared Brillouin laser using ultra-high-Q on-chip resonators. *arXiv* <https://doi.org/10.48550/arXiv.2404.06764> (2024).
  29. Chen, X. et al. High quality factor resonant metasurface with etchless lithium niobate. *Opt. Laser Technol.* **161**, 109163 (2023).
  30. Fang, C. et al. Multiple high-Q optical modes in a polymer-lithium niobate integrated metasurface. *Laser Photonics Rev.* **18**, 2300900 (2024).
  31. Regan, E. C. et al. Direct imaging of isofrequency contours in photonic structures. *Sci. Adv.* **2**, e1601591 (2016).
  32. Tang, H. et al. Experimental probe of twist angle-dependent band structure of on-chip optical bilayer photonic crystal. *Sci. Adv.* **9**, eadh8498 (2023).
  33. Tang, H. et al. Low-loss zero-index materials. *Nano Lett.* **21**, 914–920 (2021).
  34. Wang, B. et al. Generating optical vortex beams by momentum-space polarization vortices centred at bound states in the continuum. *Nat. Photonics* **14**, 623–628 (2020).
  35. Koshelev, K., Lepeshov, S., Liu, M., Bogdanov, A. & Kivshar, Y. Asymmetric metasurfaces with high-Q resonances governed by bound states in the continuum. *Phys. Rev. Lett.* **121**, 193903 (2018).
  36. Munley, C. et al. Visible wavelength flatband in a gallium phosphide metasurface. *ACS Photonics* **10**, 2456–2460 (2023).
  37. Choi, M., Munley, C., Fröch, J. E., Chen, R. & Majumdar, A. Nonlocal flat-band meta-optics for monolithic, high-efficiency, compact photodetectors. *Nano Lett.* **24**, 3150–3156 (2024).
  38. Fang, J. et al. Directional modulation of exciton emission using single dielectric nanospheres. *Adv. Mater.* **33**, 2007236 (2021).
  39. Fang, J. et al. Room-temperature observation of near-intrinsic exciton linewidth in monolayer WS<sub>2</sub>. *Adv. Mater.* **34**, 2108721 (2022).
  40. Easy, E. et al. Experimental and computational investigation of layer-dependent thermal conductivities and interfacial thermal conductance of one- to three-layer WSe<sub>2</sub>. *ACS Appl. Mater. Interfaces* **13**, 13063–13071 (2021).
  41. Zhao, Y. et al. Chirality detection of enantiomers using twisted optical metamaterials. *Nat. Commun.* **8**, 14180 (2017).
  42. Cotrufo, M., Cordaro, A., Sounas, D. L., Polman, A. & Alù, A. Passive bias-free non-reciprocal metasurfaces based on thermally nonlinear quasi-bound states in the continuum. *Nat. Photon.* **18**, 81–90 (2024).
  43. Fang, Z. et al. Nonvolatile phase-only transmissive spatial light modulator with electrical addressability of individual pixels. *ACS Nano* **18**, 11245–11256 (2024).
  44. Li, S., Ma, B., Li, Q. & Rybin, M. V. Antenna-based approach to fine control of supercavity mode quality factor in metasurfaces. *Nano Lett.* **23**, 6399–6405 (2023).
- Foundation (NSF) Grant No. DMR-2019444 and NSF-2103673. V.M.M. was also supported by NSF Grant No. DMR-2019444. Part of this work was conducted at the Washington Nanofabrication Facility / Molecular Analysis Facility, a National Nanotechnology Coordinated Infrastructure (NNCI) site at the University of Washington with partial support from NSF via awards NNCI-1542101 and NNCI-2025489. E.M.R., S.A.M. and A.A. were supported by the Simons Foundation and AFOSR Foundation. K.Y. and Y.Z. acknowledge the financial support of the National Institute of General Medical Sciences of the National Institutes of Health (R01GM146962).

## Author contributions

J.F., R.C. and A.Majumdar conceived the idea. J.F. designed the meta-resonators and experiments. E.M.R., S.A.M. and A.A. developed the analytical theories. R.C. and A.Manna fabricated the devices. A.Manna and S.P. prepared the WSe<sub>2</sub>. D.S., J.F., A.K., R.C., A.Manna and C.M. performed the experiments. J.F., E.M.R., K.Y. and Y.Z. conducted the numerical simulations. H.R., A.T. and R.C. did the morphology characterizations. J.F., R.C., D.S., V.M. and A.Majumdar interpreted the results together with all the authors. J.F. wrote the manuscript with input from all the authors and supervised the project with A.Majumdar. J.F., R.C. and D.S. contributed equally to this work.

## Competing interests

The authors declare no competing interests.

## Additional information

**Supplementary information** The online version contains supplementary material available at <https://doi.org/10.1038/s41467-024-54775-0>.

**Correspondence** and requests for materials should be addressed to Jie Fang or Arka Majumdar.

**Peer review information** *Nature Communications* thanks Nathaniel Stern and Judith Su for their contribution to the peer review of this work. A peer review file is available.

**Reprints and permissions information** is available at <http://www.nature.com/reprints>

**Publisher's note** Springer Nature remains neutral with regard to jurisdictional claims in published maps and institutional affiliations.

**Open Access** This article is licensed under a Creative Commons Attribution-NonCommercial-NoDerivatives 4.0 International License, which permits any non-commercial use, sharing, distribution and reproduction in any medium or format, as long as you give appropriate credit to the original author(s) and the source, provide a link to the Creative Commons licence, and indicate if you modified the licensed material. You do not have permission under this licence to share adapted material derived from this article or parts of it. The images or other third party material in this article are included in the article's Creative Commons licence, unless indicated otherwise in a credit line to the material. If material is not included in the article's Creative Commons licence and your intended use is not permitted by statutory regulation or exceeds the permitted use, you will need to obtain permission directly from the copyright holder. To view a copy of this licence, visit <http://creativecommons.org/licenses/by-nc-nd/4.0/>.

© The Author(s) 2024

## Acknowledgements

J.F. thanks Mr. Suichu Huang for the insightful discussion. Work at University of Washington was supported by National Science

<sup>1</sup>Department of Electrical and Computer Engineering, University of Washington, Seattle, WA 98195, USA. <sup>2</sup>Department of Physics, University of Washington, Seattle, WA 98195, USA. <sup>3</sup>Photonics Initiative, Advanced Science Research Center, City University of New York, New York, NY 10031, USA. <sup>4</sup>Physics Program, Graduate Center, City University of New York, New York, NY 10016, USA. <sup>5</sup>Walker Department of Mechanical Engineering and Texas Materials Institute, The University of Texas at Austin, Austin, TX 78712, USA. <sup>6</sup>Department of Materials Science and Engineering, University of Washington, Seattle, WA 98195, USA. <sup>7</sup>Department of Physics, City College of New York, New York, NY 10031, USA. <sup>8</sup>These authors contributed equally: Jie Fang, Rui Chen, and David Sharp.

✉ e-mail: [jiefang@uw.edu](mailto:jiefang@uw.edu); [arka@uw.edu](mailto:arka@uw.edu)